Effect of Confinement on Heat Transfer between Gas-Droplets Round Impinging Jet and Flat Plate

M.A. Pakhomov* and V.I. Terekhov
* Laboratory of Thermal and Gas Dynamics, S.S. Kutateladze Institute of Thermophysics, Siberian Branch of Russian Academy of Sciences, Novosibirsk, Acad. Lavrent'ev Av. 1, 630090, Russia

Abstract

The paper presents results of numerical study of the effect of confinement on a flow structure and heat transfer in an impinging mist jets with low mass fraction of droplets ($M_{L1}\leq 1$ %). The downward gas-droplets jet is issued from a pipe and strikes into the center of the circular target wall. Mathematical model is based on the steady-state RANS equations for the two-phase flow in Euler approximation. For the predictions of the fluctuation characteristics of the dispersed phase model equations of Zaichik et al. [1] were applied. Predictions were performed for the distances between the nozzle and the target plate $x/(2R)$=0.5–10 and the initial droplets size (d_1=5–100 μm) at the fixed Reynolds number based on the nozzle diameter, Re=26600. Addition of droplets causes significant increase of heat transfer intensity in the vicinity of the jet stagnation point compared with the one-phase air impact jet.

Introduction

Turbulent round impinging jets are widely used in many industrial applications. This has been due to high heat and mass transfer rates of the jet impingement. At cooling of turbine and electronic components, especially interesting is jet impingement occurring in a partially confined space. To design and optimize jet impingement cooling, it is essential to determine and understand the effects of such important parameters (such as nozzle-to-plate distance, Reynolds number and confinement effect). In some of previous studies (see, for example, [2-5]) these effects have been examined; however, experiments performed by different investigators are sometimes contradictory due to the differences in the initial experimental conditions.

Basic features of such flows are three flow areas (see Fig. 1): the area of free jets (1), the area of the gradient flow in the zone of critical point and the jet turn (2) and the area of wall jet (3), high rate of heat and mass transfer processes in stagnation region of the jet, significant modification of turbulent flow (see following works by [2-6]. Symbol «0» in the Fig. 1 is a stagnation point. Dyban and Mazur [3] and Jambunathan et al. [4] point out this problem and note that for a better understanding of the jet impingement heat transfer process, the details of the flow, geometry and turbulence conditions are required; only then can a comparison be made between different experimental data jets.

The development of the flow produced by confined impinging jet differs from the flow produced by unconfined impinging jet (see Fig. 1). The presence of confined surface creates a recalculating flow region below the confining plate. In unconfined and confined impinging jets heat transfer depends on a number of parameters including nozzle-to-plate distance, jet Reynolds number and geometry of the nozzle. The impinging jet flow, despite its relatively simple geometry, exhibits extremely complex flow characteristics. The flow in stagnation region is nearly irrotational and there is a large total strain along the streamline. It turns in the radial direction with substantial curvature. Away from this region, the flow forms wall jet boundary layers along the heat transfer plate.

Industrial applications, especially in electronic cooling, often required the jet to be confined by a solid wall at the level of the jet nozzle exit cross-section.

The use of a gas-droplets mist impinging jet is one of the efficient methods of surface cooling augmentation. The method providing significant increase of heat and mass transfer rate between the wall and impact jet flow applies two-phase gas-droplets heat carriers as a coolant. An accurate prediction of flow and concurrent heat transfer in the mist jet impingement poses a significant problem. Two-phase mist heat carriers increase heat transfer several times (see, for instance, works [7-12].

Modeling of heat transfer in the plane vapor-droplets impact jet was performed in the works [8, 11]. Simulations were provided with the use of CFD code FLUENT. Water droplets, less than 15 μm diameter and at concentrations below 10 percent of mass, are considered. The heat transfer is assumed to be the superposition of three components: heat flow to the steam, heat flow to the dispersed mist, and heat flow to the impinging droplets. The latter is modeled as heat flow to a spherical cap for a time dependent on the droplet size, surface

* Corresponding author: pakhomov@ngs.ru

tension, impact velocity and surface temperature. The model is used to interpret experimental results for steam invested with water mist in a confined slot jet.

In [9] detailed numerical study of the round impact gas-droplets jet was carried out with the use of commercial CFD FLUENT package. The gas phase is described with RANS method taking into account the coupling between the phases. For the description of droplets dynamics Lagrange approach was applied. The authors used for the closure several turbulence LEVM: "standard" k–ε, k–ω by Menter, RNG k–ε, incorporated into the FLUENT. In the calculations the realizable k–ε model was used as the one that describes the jet dynamics more accurately. With the method Volume of Fluid (VOF) influence of the form of the single droplet on heat transfer at its contact with the surface was studied in details. In the paper [9] the case of the same temperature of the plate surface and the particles was investigated; and only heat transfer between gas and wall was considered (difference between gas and droplets/wall temperatures equaled 20^0). The using of small difference between the wall and gas flow temperatures allowed to not considering the effect of gas phase thermophysical properties on the transport process in the gas phase. The employment of the model in this case was more confined. Effect of main thermogasdynamic parameters such as droplets mass fraction, their size, two-phase flow velocities, nozzle diameter and distance from the nozzle to the plate on heat transfer between flat surface and two-phase flow has been investigated. For the case of large mass concentrations of droplets it is necessary to consider influence of heat transfer at drop contact with the wall, described with VOF method. For the case of small concentrations of disperse phase the results are reasonable only at consideration of heat transfer intensification at drop evaporation in the gas flow.

The main aims of this paper were to carry out numerical study of effect of droplets evaporation on the flow and heat transfer in the impact mist spray at varying basic thermogasdynamic parameters of two-phase flow, i.e. distance from the nozzle to the plate, droplets diameter, wall temperature and its mass fraction in cases of unconfined and confined geometry.

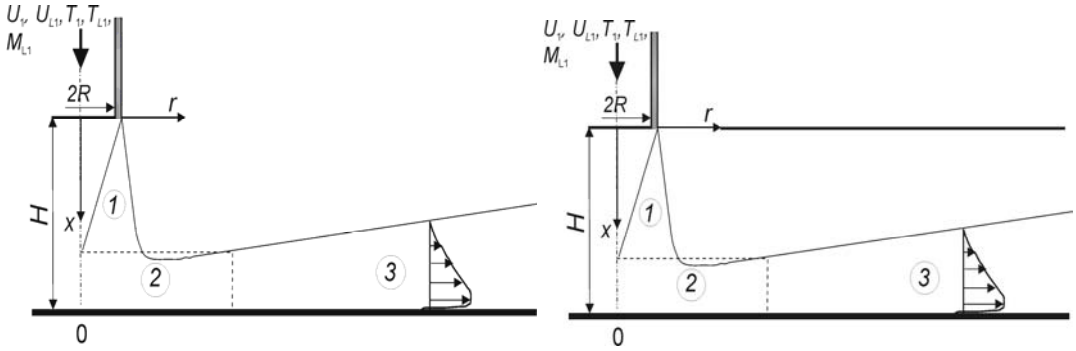

Figure 1. Schematic representation of studied cases for unconfined (a) and confined (b) impinging jet

Mathematical Model

The numerical model is based on the Eulerian/Eulerian approach. For the gas phase we used the set of steady-state, axisymmetric RANS equations in connection with an appropriate turbulent k–$\tilde{\varepsilon}$ model by Hwang and Lin [13]. The set of equations includes continuity, momentum, energy, mass concentration of vapor equation in binary gas-vapor mixture [12]

$$\rho\frac{\partial U_j}{\partial x_j}=\frac{6J\Phi}{d}$$

$$\rho\frac{\partial\left(U_iU_j\right)}{\partial x_i}=-\frac{\partial\left(P+2k/3\right)}{\partial x_i}+$$

$$+\frac{\partial}{\partial x_j}\left[\left(\mu+\mu_T\right)\left(\frac{\partial U_i}{\partial x_j}+\frac{\partial U_j}{\partial x_i}\right)\right]-\left(U_i-U_{Li}\right)\frac{\Phi}{d}\times\left[\frac{1}{8}C_D\rho\left|\vec{U}-\vec{U}_L\right|+J\right]+\rho_L g_u<u_iu_j>\frac{\partial\Phi}{\partial x_j}$$

$$\rho\frac{\partial\left(U_i T\right)}{\partial x_i}=\frac{\partial}{\partial x_i}\left(\frac{\mu}{\mathrm{Pr}}+\frac{\mu_T}{\mathrm{Pr}_T}\right)\frac{\partial T}{\partial x_i}-\frac{6\Phi}{C_P d}\left[\alpha\left(T-T_L\right)+JL\right]+\frac{\rho D_T}{C_P}\left(C_{PV}-C_{PA}\right)\left(\frac{\partial K_V}{\partial x_i}\frac{\partial T}{\partial x_i}\right)+\frac{C_{PL}\rho_L\tau g_{ut}}{C_P}<u_j t>\frac{\partial\Phi}{\partial x_j}$$

$$\rho\frac{\partial\left(U_i K_V\right)}{\partial x_i}=\frac{\partial}{\partial x_i}\left(\frac{\mu}{\mathrm{Sc}}+\frac{\mu_T}{\mathrm{Sc}_T}\right)\frac{\partial K_V}{\partial x_i}+\frac{6J\Phi}{d}$$

$$\rho=P/\left(\bar{R}T\right). \tag{1}$$

Value of turbulent Prandtl and Schmidt numbers were equal to $\mathrm{Pr}_T=\mathrm{Sc}_T=0.85$.

Despite the deficiency in the method based on RANS equations with LEVM k–$\tilde{\varepsilon}$ turbulence models it turns out to be the major for the most of engineering implementations and will be used in this work for impact gas-droplets jet modeling. The adoption of the Taylor microscale in the damping functions and the inclusion of pressure diffusion terms in both the k and $\tilde{\varepsilon}$ equations were key features of this model. Durbin's correction [14] is applied in the work for the appropriate k–$\tilde{\varepsilon}$ model. To improve the behavior of the model [13], a realizability constraint is applied on the turbulent time scale in the equation for $\tilde{\varepsilon}$.

The equations for turbulent kinetic energy (TKE) and rate of its dissipation modified for the case of present dispersed phase are given below

$$\rho\frac{\partial\left(U_j k\right)}{\partial x_j}=\frac{\partial}{\partial x_j}\left[\left(\mu+\frac{\mu_T}{\sigma_k}\right)\frac{\partial k}{\partial x_j}\right]-\frac{1}{2}\frac{\partial}{\partial x_j}\left[\mu\frac{k}{\varepsilon}\frac{\partial\hat{\varepsilon}}{\partial x_j}\right]+\rho\Pi-\rho\varepsilon+S_k,$$

$$\rho\frac{\partial\left(U_j\tilde{\varepsilon}\right)}{\partial x_j}=\frac{\partial}{\partial x_j}\left[\left(\mu+\frac{\mu_T}{\sigma_\varepsilon}\right)\frac{\partial\tilde{\varepsilon}}{\partial x_j}\right]+\frac{\partial}{\partial x_j}\left(\mu\frac{\tilde{\varepsilon}}{k}\frac{\partial k}{\partial x_j}\right)+\frac{\rho\tilde{\varepsilon}}{k\Lambda}\left(C_{\varepsilon 1}f_1\Pi-C_{\varepsilon 2}\tilde{\varepsilon}f_2\right)+S_\varepsilon \tag{2}$$

$$\mu_T=\frac{\rho C_\mu f_\mu}{1+\left(\Pi/\tilde{\varepsilon}-1-A_k/\tilde{\varepsilon}\right)/E}\frac{k^2}{\tilde{\varepsilon}} \tag{3}$$

Here S_k and S_ε in Eqs. (1) are source/sink terms which take into account the effect of dispersed phase on TKE of the gas and have the form [15]; $\Lambda=\dfrac{1.2}{3f_\mu C_\mu\sqrt{2S_{ij}S_{ij}}}$ is the Durbin's correlation [14] in the case of 2D flow; $\Pi=-\rho<u_i u_j>\dfrac{\partial U_i}{\partial x_j}$ is the production of turbulent energy caused by shear; $S_{ij}=\dfrac{1}{2}\left(\dfrac{\partial U_j}{\partial x_i}+\dfrac{\partial U_i}{\partial x_j}\right)$ is the local strain rate tensor and C_μ and f_μ are damping constants of the model [13]. $A_k=\dfrac{2M_L k}{\tau}\left(1-f_u\right)-g_u<u_i u_k>\left(U_i-U_{Li}\right)\dfrac{\partial M_L}{\partial x_k}$ [1], where $f_u=1-\exp\left(-\Omega^L/\tau\right)$; $g_u=\exp\left(-\Omega^L/\tau\right)-f_u$. In the Eq. (3) E=2 is constant of Rotta's approximation. This modification of the expression (3) does not change the equation of turbulence model.

The model used Euler/Euler approach for both phases. The system of mean equations for the transport process in dispersed phase has the form

$$\frac{\partial U_{Lj}}{\partial x_j}=-\frac{6J\Phi}{d}$$

$$\rho_L\frac{\partial\left(\Phi U_{Lj}U_{Li}\right)}{\partial x_j}+\rho_L\frac{\partial\left(\Phi<u_{Li}u_{Lj}>\right)}{\partial x_j}=\Phi\left(U_i-U_{Li}\right)\frac{\rho_L}{\tau}+\Phi\rho_L g-\frac{\rho_L}{\tau}\frac{\partial\left(D_{Lij}\Phi\right)}{\partial x_j}$$

$$\rho_L\frac{\partial\left(\Phi U_{Lj}T_{Li}\right)}{\partial x_j}+\rho_L\frac{\partial}{\partial x_j}\left(\Phi<\theta u_{Lj}>\right)=\Phi\left(T_i-T_{Li}\right)\frac{\rho_L}{\tau_\Theta}-\frac{\rho_L}{\tau_\Theta}\frac{\partial\left(D^\Theta_{Lij}\Phi\right)}{\partial x_j}. \tag{4}$$

Here D_{Lij} and D^Θ_{Lij} in Eqs. (4) are tensors of turbulent diffusion and turbulent heat flux of particles [1].

For predictions of Reynolds stress components $\left\langle u_{Li}u_{Lj}\right\rangle$, turbulent heat flux $\left\langle\theta_L u_{Lj}\right\rangle$ and temperature fluctuations $\left\langle\theta_L^2\right\rangle$ in the dispersed phase fluctuations were used model by Zaichik et al. [1]

$$U_{Lk}\frac{\partial\left\langle u_{Li}u_{Lj}\right\rangle}{\partial x_k}+\frac{1}{\Phi}\frac{\partial}{\partial x_k}\left(\Phi\left\langle u_{Li}u_{Lj}u_{Lk}\right\rangle\right)+\left\langle u_{Li}u_{Lk}\right\rangle\frac{\partial U_{Lj}}{\partial x_k}+\left\langle u_{Lj}u_{Lk}\right\rangle\frac{\partial U_{Li}}{\partial x_k}=\frac{2}{\tau}\left(f_u\left\langle u_iu_j\right\rangle-\left\langle u_{Li}u_{Lj}\right\rangle\right)$$

$$U_{Lk}\frac{\partial\left\langle \theta_Lu_{Lj}\right\rangle}{\partial x_k}+\frac{1}{\Phi}\left\{\frac{\partial}{\partial x_k}\left(\Phi\left\langle \theta_Lu_{Li}u_{Lk}\right\rangle\right)\right\}+\left\langle u_{Li}u_{Lk}\right\rangle\frac{\partial T_L}{\partial x_k}+\left\langle \theta_Lu_{Lk}\right\rangle\frac{\partial U_{Li}}{\partial x_k}=$$

$$=\left(\frac{f_{\Theta u}}{\tau}+\frac{f_{u\Theta}}{\tau_\Theta}\right)\left\langle u_it\right\rangle-\left(\frac{1}{\tau}+\frac{1}{\tau_\Theta}\right)^{-1}\left\langle \theta_Lu_{Lj}\right\rangle.$$

$$U_{Lk}\frac{\partial\left\langle \theta_L^2\right\rangle}{\partial x_k}+\frac{1}{\Phi}\left\{\frac{\partial}{\partial x_k}\left(\Phi\left\langle \theta_L^2u_{Lk}\right\rangle\right)\right\}+2\left\langle \theta_Lu_{Lk}\right\rangle\frac{\partial T_L}{\partial x_k}=\frac{2}{\tau_\Theta}\left(f_{ut}\left\langle t^2\right\rangle-\left\langle \theta_L^2\right\rangle\right). \quad (5)$$

Here f_u, and f_{ut} are coefficients of droplets entrainment into a large-eddy fluctuational motion of the gas phase.

Both the droplets deposition on the wall and the heat transfer due to the contact of droplets with the wall were taken into account. The droplets were assumed to undergo instantaneous evaporation on the wall, with no liquid film formed on it.

Numerical Realization and Boundary Conditions

The discretization of the transport equations in the computational domain was performed by the use of the finite-volume techniques by Patankar [16]. The QUICK scheme [17] was used for convective fluxes and the central differences – for diffusion fluxes. The SIMPLEC solution algorithm by Van Doormal and Raithby [18] was adopted for pressure-velocity coupling. All computations were performed on the grid comprising 250×200 control volumes (CV) with higher resolution in the wall and axis regions. At least 10 CVs have been generated to resolve the mean velocity field and turbulent quantities in the viscosity-affected near-wall region. The nearest to the wall point was located at y_+=1.

The mesh configuration was tested to be sufficient to provide grid independent results. Additionally, a series of test computations for a gas-droplet flow occupying totally 350×300 CVs was performed. The local Nusselt numbers in different computation runs differed within 1 % for the single-phase flow and within 2 % for the gas-droplet flow with evaporating droplets. The computational domain is 20R. Here, R is the jet nozzle radius.

In order to resolve the steep gradient of the flow variable near the wall, a non-uniform grid clustered at both walls was used. The grid is refined near the symmetry axis (in order to have sufficient accuracy near the stagnation point). At least 10 CVs have been generated to resolve the mean velocity field and turbulent quantities in the viscosity-affected near-wall region. The nearest to the wall point was located at y_+=1. The computational domain was 20R. Here, R is the jet nozzle radius.

A fully developed turbulent pipe single-phase flow (separately computed) was imposed at the inlet boundary, while static pressure was extrapolated from the flow field. Droplets injected on the nozzle exit cross-section over the whole pipe radius. The turbulence level was set to 1%. A zero derivative is used for the static pressure.

At walls, no-slip and impermeability conditions were used for the velocity components. The turbulent kinetic energy are set to zero and constant temperature conditions was used for target wall T_W=const. For the confined wall we used condition for an adiabatic wall. The value of dissipation rate at walls was determined as in [13]: $\varepsilon_W=2\nu\left(\partial\sqrt{k}/\partial y\right)^2$. For the dispersed phase mean velocity components and its fluctuations we utilize the boundary conditions of [1]. For droplets temperature and its fluctuations was used the boundary conditions as in the paper [21].

All other boundary conditions are standard.

Comparison with Experimental and Numerical Results for the Single-Phase Impinging Jet

To compare the experimental data on dynamics and heat transfer of the impact air jet we used the works [19, 20, 21] for single-phase air jet. In addition, our results were compared with V2F turbulence model of Behnia et al. [22], NLEVM by Dick and Merci [23], and LES predictions by Volkov [24].

The distributions of Nusselt number for one-phase air flow in the distance $x/(2R)$=2 and 6 from the nozzle cross-section were presented in the Fig. 2. The results of our simulations satisfactory described the measured distributions of heat transfer coefficient. The presence of the second local maximum of Nu number was typical for the measurements and predictions in other papers. In our calculations this maximum is not so apparent. Minimum value of heat transfer lies at $r/(2R)\approx1.5$, that is specific for experiments and simulations [19, 20]. The computations according to the "standard" k–ε model gives almost two times overpredicted Nusselt number in the

stagnation point compared with the data of measurements and simulations of other authors and our results according to the model [13] with Durbin's correction [14]. For the distance $x/(2R)$=6 between nozzle and target surface (see Fig. 2b) both for the data of our predictions and the results of other works the typical was the absence of the second maximum in the Nusselt number profile.

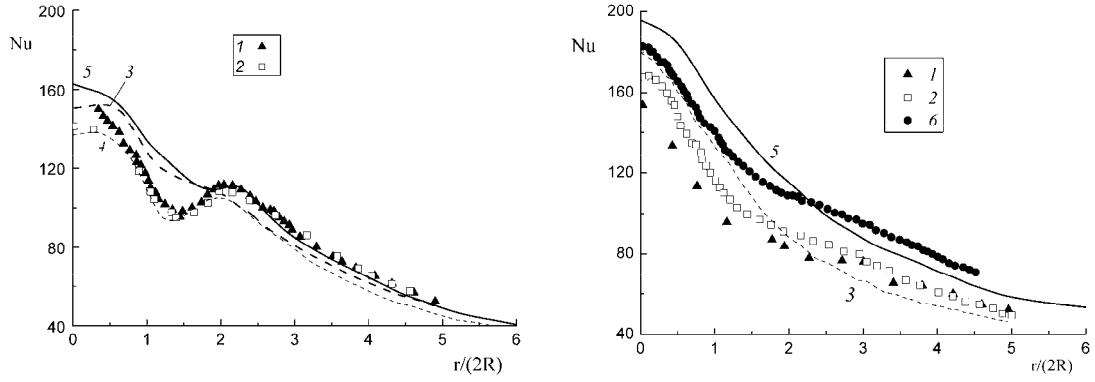

a b

Figure 2. Nusselt number profiles at the flat plate for $H/(2R)$=2 (a) and 6 (b) and Re=23000. *1*, *2, 6* – measurements of [19, 20] respectively; *3*, *4* – predictions by V2F turbulence model of [21] and LES by [23] (dashed lines), *5* – computations by authors (solid lines)

Main conclusions derived from these test computations are as follows. The steady-state RANS model with LEVM Hwang and Lin [13] and Durbin's correction [14] can qualitatively and correctly describe complex regularities of heat transfer in single-phase impact jet flows.

Numerical Results for Mist Jet Impingement

All simulations were carried out for the mixture of water droplets and air with atmosphere pressure. In the inflow section (nozzle section) profiles of the gas phase parameters are set on the basis of preliminary predictions of the single-phase flow in the pipe with the length 150R. In the initial cross-section droplets were monodisperse, downstream from the nozzle exit their size changed in both directions due to evaporation. The size of the dispersed phase was d_1=1–200 μm. The initial mass fraction of water droplets was M_{L1}=0–1 %. The diameter of the nozzle was $2R$=20 mm. Gas phase velocity on the nozzle exit cross-section was U_1=20 m/s, the Reynolds number Re=$U_1 2R/\nu \approx 26600$. Initial droplets velocity was $U_{Lm}=0.8U_m$. The wall temperature was T_W=353–473 K and was realized a boundary condition T_W=const. Gas and droplets initial temperature was $T_1=T_{L1}$=293 K and steam mass fraction in the gas/vapor mixture in the jet and in ambient medium was $M_{V1}=M_{Ve}$=0.01%. The nozzle-to-plate distance varied in the range $H/(2R)$=0.25–10.

Flow structure

Profiles of axial and radial components of gas and disperse phases velocities normalized by the value of gas velocity on jet axis on the nozzle edge for two nozzle-to-plate distances were shown in Fig. 3 at $H/(2R)$=2. On the left of all figures there are results for the single-phase impact jet and on the right – for two-phase flow. At the distance from the nozzle $x/(2R)$=1.5 widening of the mist turbulent jet is a little more than the single-phase and the profile of the longitudinal velocity is qualitatively similar to the one in the free jet. Lead of the two-phase jet over one-phase is mainly explained by additional generation of the impulse from the particles and insignificantly from their evaporation. In the wall region $x/(2R)$=1.9 the effect of the wall is already pronounced and the value of axial velocity of gas and droplets significantly decreases (see Figs. 3d). The velocity of particles is higher than the gas velocity owing to inertia action. Results given in the Fig. 4 have the qualitatively similar form.

Profiles of mass concentration of the dispersed phase and steam downstream from the nozzle exit cross-section are given in the Figs. 4 and 5 for two distances $H/(2R)$=2 (a) and $H/(2R)$=6 (b), respectively. Initial profiles of droplets and vapor concentration on the nozzle exit cross-section were uniform (*1*). The droplets mass fraction decreases for the account of the jet spread and droplets evaporation (*2*, *3*) along the jet axis. The profile of the particles mass concentration in the near-wall zone (*4*) undergoes considerable change ($M_L/M_{L1}\approx 0.5$ for $H/(2R)$=2 and $M_L/M_{L1}\approx 0.2$ for $H/(2R)$=6) due to significant jet spread in the vicinity of the stagnation point and intense evaporation of droplets in the wall region.

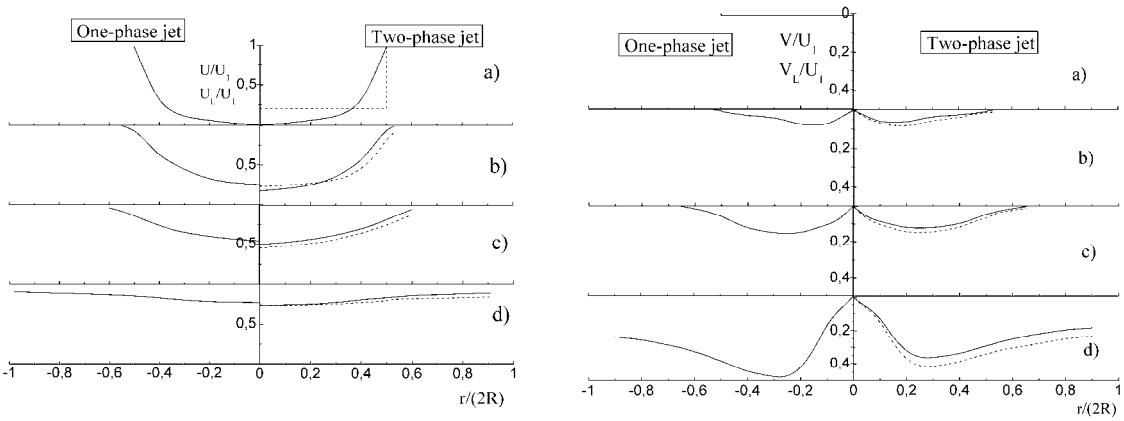

Figure 3. Distribution of axial U/U_1 and radial V/U_1 velocities of gas phase (solid lines) and droplets (dashed lines) downstream of the jet nozzle for $H/(2R)$=2. Solid lines are gas phase, dashed curves are droplets. (a) – $x/(2R)$=0, (b) – 0.5, (c) – 1.5, (d) – 1.9

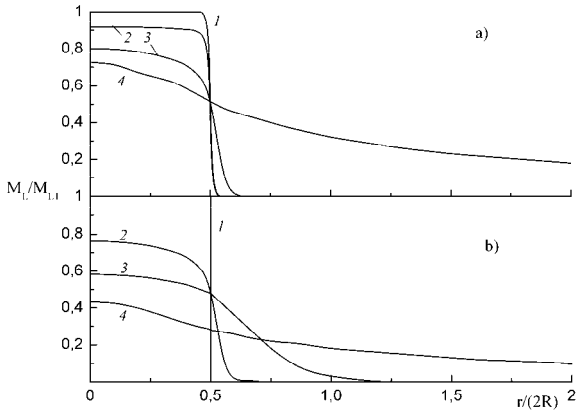

Figure 4. Distribution of droplets mass fraction along the flat plate length for $H/(2R)$=2 (a) and 6 (b). Re=26600, M_{L1}=1 %, d_1=50 μm. (a): *1* – $x/(2R)$=0, *2* – 0.5, *3* – 1.5, *4* – 1.9; (b):, *1* – $x/(2R)$=0, *2* – 1.5, *3* – 4, *4* – 5.9

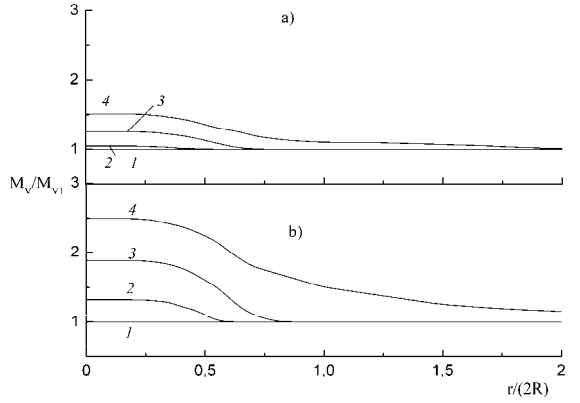

Figure 5. Profiles of steam mass fraction over the plate surface for $H/(2R)$=2 (a) and 6 (b). Conditions and designations adopted in the predictions are the same as in Fig. 4

Heat transfer

The effect of droplets mass fraction on heat transfer intensification was shown in the Figs. 5 for two nozzle-to-plate distances $H/(2R)$=2 (Fig. 5a) and $H/(2R)$=6 (Fig. 5b). Here Nu_A is the Nusselt number for the air impinging jet. Droplets mass fraction (see Figs. 5a and 6a) increased for the account of intensified evaporation

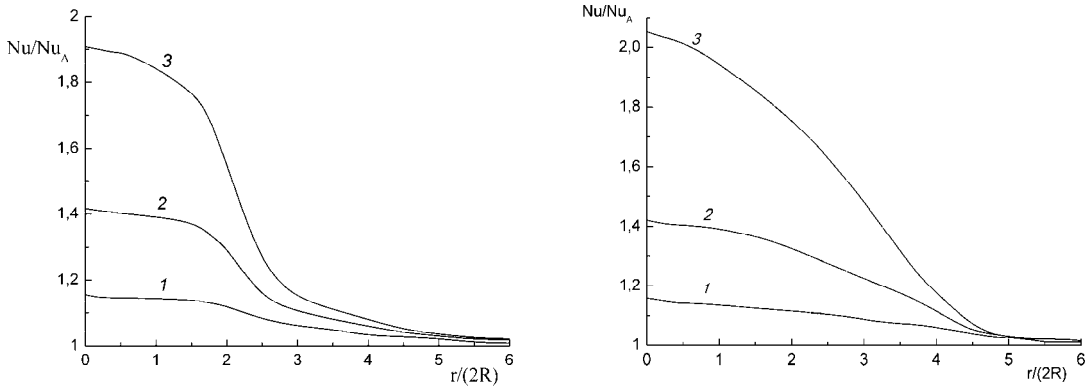

Figure 6. Nusselt number enhancement ratio downstream of stagnation point for various droplets mass fraction for nozzle-to-plate distance $H/(2R)$=2 (a) and $H/(2R)$=6(b). d_1=50 μm, *1* – M_{L1}=0.2 %, *2* – 0.5 %, *3* – 1 %.

processes (more than two-fold compared to the single-phase air impinging jet) results in the increase of heat transfer between the jet and the impingement wall in the stagnation region ($r/(2R)$<2). The maximum Nusselt number was observed around the stagnation region for all droplet mass fractions. In the area of wall jet propagation (at the distance $r/(2R)$>2), the Nusselt number of gas-droplets flow coincides with the heat transfer coefficient Nu_A in the single-phase impinging jet flow. This is explained by the jet mixing with ambient environment and droplets evaporation and correlates with the numerical predictions of [9]. All peculiarities of heat transfer in mist impact jets pointed out in the Figs. 5 and 6 are specific for both distances between the nozzle and the plate studied in the paper.

Confined mist jet

All previous computations were performed for the unconfined geometry. Numerous experiments and predictions for the single-phase jet (for example, see [25-29]) aimed at investigation of the confinement wall effect on the jet structure and stagnation heat transfer and study of the flow physics in the single-phase jet and correlation of unconfined geometry applied to confined configuration. Authors observed from 5 to 20 % reduction in the average heat transfer rate and the effect of confinement specific only for small nozzle-to-plate distance ($H/(2R)\leq 0.5$).

The numerical model developed in the paper demonstrates rather good results for the unconfined mist jet. We believe that the model is accurate enough to compute the gas-droplets jet with confinement. We varied the nozzle-to-plate distance in confined jet and compared to the results obtained for the unconfined configuration.

The friction coefficient is shown in the Fig. 7 for the single-phase flow (on the left) and for the gas-droplets flow (on the right). The effect of the solid top wall is more noticeable only for small nozzle-to-plate distances ($H/(2R)\leq 1$). The friction in the confined jet is lower than the one in the unconfined impinging jet. For rather high nozzle-to-plate spacing ($H/(2R)$>2), the confinement had no effect on the friction coefficient distribution both in the single-phase and mist flows. These phenomena were observed both for the single-phase and two-phase flows. No gas phase was entrained from the upper boundary because of the solid confinement wall. The mass flux decreased, and the bulk velocity was much lower in the confined impinging jet. The same trends were observed in the case of evaporating mist jet.

The Fig. 8 shows the Nusselt number profiles for different nozzle-to-plate distances. The presence of a top solid wall created a recirculation region. The trends observed in the heat transfer rate distributions were same to the ones in the wall friction coefficient profiles (see Fig. 7). The confinement effect on the Nusselt number distributions was noticeable only for the small nozzle-to-plate spacing for the single-phase and mist impinging jet. For the $H/(2R)\leq 1$, the heat transfer profiles in the one-phase and two-phase confined flows differed from the ones in the unconfined jet. The Nusselt number coefficient was lower for the confined jet. This was proved by measurements in [25, 26, 29] and predictions of Behnia et al. [27] for the single-phase impinging jets. The top wall develops resistance to the flow rising along with the nozzle-to-plate distance decrease. Entrainment of the ambient gas by the jet diminishes the impingement heat transfer. Gas temperature in the confined configuration

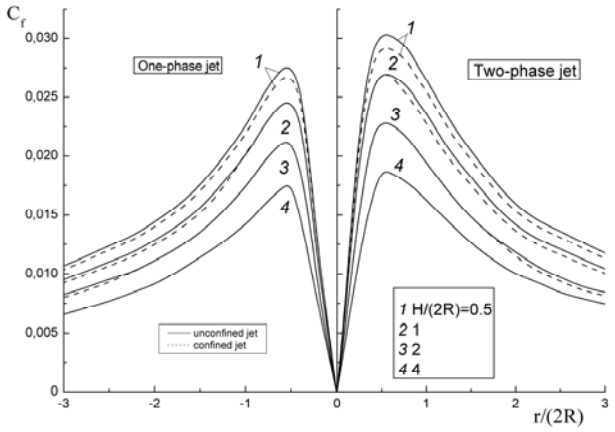

Figure 7. Profiles of friction coefficient for various nozzle-to-plate distances. Solid lines are unconfined jet, dashed lines are confined jet. *1* – *H*/(2*R*)=0.5, *2* – 1, *3* – 2, *4* – 4

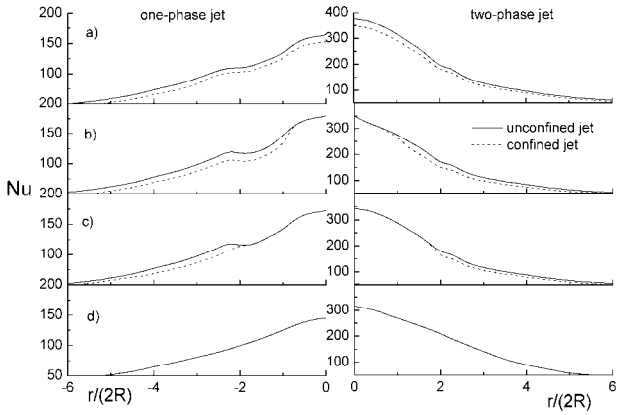

Figure 8. Distributions of Nusselt number in the confined (dashed curves) and unconfined (solid curves) mist impinging jets. (a) – *H*/(2*R*)=0.5, (b)– 1, (c) – 2, (d) – 4

is not equal to the ambient medium temperature. The gas is heated up and the mean gas temperature in the confined section becomes larger than in the unconfined geometry.

Comparison with Experimental Results

The Fig. 9 gives a comparison between our predictions and data for steam-droplets impinging confined jet of Li et al. [8]. Here *B* is the nozzle width. Predictions have been made at the following conditions: *B*=7.5 mm; Reynolds number Re=14000; density of the heat flow on the plate wall q_W=7.54 kW/m^2; mass concentration of water droplets M_{L1}=0.015; temperature of saturated vapor T_{Sat}=105 ^{0}C and initial diameter of droplets d_1=7 μm.

Note that the wall temperature according to the measurements data and our calculations in case of vapor and droplets flow have always been above 120 ^{0}C, that proves absence of the film from deposited droplets on its surface. It is worth mentioning over 2.5 times increase of the heat transfer intensification parameter (according to the measurement data) and over 2.1–2.2 times (according to computation data). Agreement between our computation results and numerical and measurements data of Li et al. [8] was quite good.

The Fig. 10 demonstrates comparison of our predictions and data for the mist impinging unconfined jet obtained by Kanamori et al. [10]. Experiments were performed at the following conditions: the nozzle diameter 2*R*=51 mm, Reynolds number Re=$U_1 2R/\nu$=5×10^4; density of heat flux on the plate surface q_W=1.4 kW/m^2; mass concentration of water droplets M_{L1}=0–0.5 %, initial temperature T_1=293 K and initial diameter of the drops d_1=14 μm. The impact jet was directed upward.

Use of gas-droplets mist impact flow as a coolant results in significant growth of heat transfer intensity (more than 2.5 times compared to the one-phase impact jet) (lines *3*, *4*). Note that main increase of heat transfer rate in the experiments [10] falls on the gradient area that proves our numerical results. Computation results and numerical and measurements data agreed rather well.

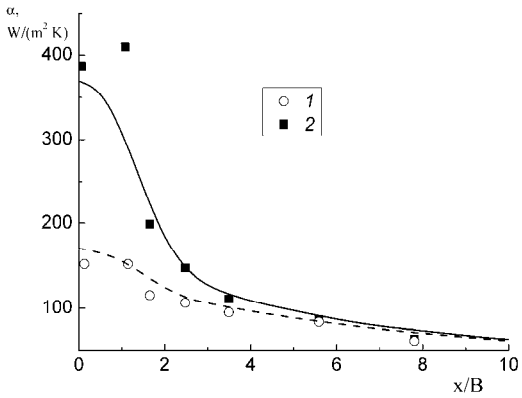

Figure 9. Heat transfer in the steam-droplets confined impinging jet. Symbols are the measurements results [8], curves are the predictions of this paper. Dashed curve is the simulation for single-phase flow. *1* – single-phase steam jet, *2* – two-phase jet

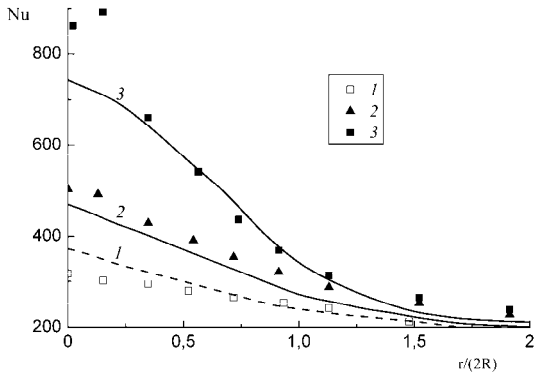

Figure 10. Heat transfer in the mist unconfined impinging jet. Symbols are the measurements results [10], curves are the predictions of this paper. Dashed line is the simulation for single-phase flow. *1* – single-phase flow, *2* – M_{L1}=0.05 %, *3* – 0.1, *4* – 0.15

Conclusions

Mathematical model using Euler/Euler description for both phases was developed for flow and heat and mass transfer processes in the impact two-phase jet. It is shown that employment of linear eddy-viscosity model by Hwang and Lin [13] with Durbin's correction [14] enabled qualitatively true prediction of heat transfer at mist impinging jet.

Droplets addition substantially increases heat transfer rate (several times) compared to the one-phase air impact jet due to the droplets evaporation. The effect of confinement on the local heat transfer behavior in the mist flow has been studied. It has been shown that confinement decreases the average heat transfer rate, but the change of the local heat transfer coefficient in the stagnation point is insignificant. The effect of confinement on the heat transfer is considerable only in very small nozzle-to-plate distances ($H/(2R)<0.5$) both in single-phase and mist impinging jets.

Acknowledgments

This work was partially supported by the Russian Foundation for Basic Research (Projects No. 09-08-00197) and by the Russian Federation's Presidental Foundation for Young PhD Scientists (Grant MK-.2010.8).

Nomenclature

α heat transfer coefficient [$Wm^{-2}K^{-1}$]
r radial coordinate [m]

Subscripts
1 parameter under initial conditions
A single-phase air impinging jet
L droplet
V vapor
e parameter under ambient medium conditions

Acronym
LEVM linear eddy viscosity model
LRN low Reynolds number
NLEVM non-linear eddy viscosity model
RSM Reynolds stress model
VOF volume of fluid

References

[1] Zaichik L.I., Pershukov V.A., Kozelev M.V., Vinberg A.A., *International J. Exp. Thermal and Fluid Sci.* 15:291–310. (1997)
[2] Martin, K., *Adv. Heat Transfer* 13:1–60(1977).
[3] Dyban E.P., Mazur A.I., *Convective Heat Transfer in Jet Flows Around Bodies*, Naukova Dumka, 1982, (in Russian).
[4] Jambunathan, K., Lai, E., Moss, M.A., and Button, B.L., *International J. Heat and Fluid Flow* 13:106–115 (1992).
[5] Webb, B.W., and Ma, C.F., *Adv. in Heat Transfer* 26:10 5–217 (1995).
[6] Zuckermann, N, and Lior, N., *Trans. ASME J. Heat Transfer* 127:544–552 (2005).
[7] Buyevich, Yu.A., and Mankevich, V.N., *International J. Heat and Mass Transfer* 39:2353–2362 (1996).
[8] Li, X., Gaddis, J.L., and Wang, T., *Trans. ASME J. Heat Transfer* 124:1086–1092 (2001).
[9] Garbero, M., Vanni, M., and Fritsching, U., *International J. Heat and Fluid Flow* 27:105–122 (2006).
[10] Kanamori, A., Hiwada, M., Minatsu, J., Sugimoto, H., and Oyakawa, K., *Second International Conference on Jets, Wakes and Separated Flows ICJWSF-2008*, Berlin, Germany. September 2008. CD-disc. 9 p.
[11] Wang, T., and Dhanasekaran, T.S., *ASME Turbo Expo 2008: Power for Land, Sea and Air GT2008*, May 2008, Berlin, Germany, CD-disc. 14 p.
[12] Pakhomov, M.A., and Terekhov, V.I., *Sixth International Symposium on Turbulence, Heat and Mass Transfer*, Rome, Italy. September 2009. Paper E-031. CD-disc. 12 p.
[13] Hwang, C.B., and Lin, C.A., *AIAA J.* 36:38–43 (1998).
[14] Durbin, P.A., *International J. Heat and Fluid Flow* 17 (1996) 89–90.
[15] Terekhov, V.I., and Pakhomov, M.A., *International J. Thermal Science,* 43:595–610 (2004).
[16] Patankar, S.V., *Numerical Heat Transfer and Fluid Flow*, Hemisphere, New York, (1980).
[17] Leonard, B.P., *Computational Methods Applied Mechanical Engineering* 19:59–79 (1979).
[18] Van Doormaal, J.P., and Raithby, G.D., Int. J. Numerical Heat Transfer. Part A 7 (1984) 147–164.
[19] Baughn, J.W., and Shimizu, S., *Trans. ASME J. Heat Transfer* 111:1096–1098 (1989).
[20] Baughn, J.W., Hechanova, A., and Yan, X., *Trans. ASME J. Heat Transfer* 113:1023–1025 (1991).
[21] Cooper, D., Jackson, D.C., Launder, B.E., and Liao, G.X., *International J. Heat and Mass Transfer* 36:2675–2684 (1993).
[22] Behnia, M., Parneix, S., and Durbin, P.A., *International J. Heat and Mass Transfer* 41:1845–1855 (1998).
[23] Merci, B., and Dick, E., *International J. Heat and Mass Transfer* 46:469–480 (2003).
[24] Volkov, K.N., *High Temperature* 45:818–825 (2007).
[25] Obot, N., Mujumdar, A., and Douglas, W., *Seventh International Heat Transfer Conference IHTC-7*, Munich, Germany. 1982 3:395–400.
[26] Garimella, S.V., and Rice, R.A., *Trans. ASME J. Heat Transfer* 117:871–877 (1995).
[27] Behnia, M., Parneix, S., Shabany, Y., and Durbin, P.A., *International J. Heat and Fluid Flow* 20:1–9 (1999).
[28] Brignoni, L.A., and Garimella, S.V., *International J. Heat and Mass Transfer* 43:1133–1139 (2000).
[29] Gao, N., and Ewing, D., *International J. Heat and Fluid Flow* 27:33–41 (2006).